OPEN ACCESS
JOURNAL OF ADVANCED DIELECTRICS
Vol. 13, No. 1 (2023) 2242005 (11 pages)

DOI: 10.1142/S2010135X2242005X

Ultra-fast charge-discharge and high-energy storage performance realized in $K_{0.5}Na_{0.5}NbO_3$-$Bi(Mn_{0.5}Ni_{0.5})O_3$ ceramics

Xinru Nie[*], Yan He[*], Qiangqiang Shi[*], Yuqian Liang[*], Lingling Wei[*], Pengfei Liang[†], Xiaolian Chao[*,‡,§], Guoxin Hu[*,**] and Zupei Yang[*,††]

[*]*Key Laboratory for Macromolecular Science of Shaanxi Province, Shaanxi Key Laboratory for Advanced Energy Devices, Shaanxi Engineering Laboratory for Advanced Energy Technology School of Materials Science and Engineering Shaanxi Normal University, Xi'an, 710062, Shaanxi, P. R. China*

[†]*School of Chemistry and Chemical Engineering, Shaanxi Normal University Xi'an, 710062, Shaanxi, P. R. China*

[‡]*School of Physics and Information Technology, Shaanxi Normal University, Xi'an 710062, Shaanxi, P. R. China*

[§]chaoxl@snnu.edu.cn
[**]huguoxin@snnu.edu.cn
[††]yangzp@snnu.edu.cn

Received 27 September 2022; Revised 23 October 2022; Accepted 2 November 2022; Published 17 February 2023

Lead-free relaxor ceramics $(1-x)K_{0.5}Na_{0.5}NbO_3 - xBi(Mn_{0.5}Ni_{0.5})O_3$ ($(1-x)$KNN-xBMN) with considerable charge–discharge characteristics and energy storage properties were prepared by a solid state method. Remarkable, a BMN doping level of 0.04, 0.96KNN–0.04BMN ceramic obtained good energy storage performance with acceptable energy storage density W_{rec} of 1.826 J/cm^3 and energy storage efficiency η of 77.4%, as well as good frequency stability (1–500 Hz) and fatigue resistance (1–5000 cycles). Meanwhile, a satisfactory charge–discharge performance with power density P_D ~ 98.90 MW/cm^3, discharge time $t_{0.9}$ < 70 ns and temperature stability (30–180°C) was obtained in 0.96KNN–0.04BMN ceramic. The small grain size (~150 nm) and the high polarizability of Bi^{3+} are directly related to its good energy storage capacity. This work proposes a feasible approach for lead-free KNN-based ceramics to achieve high-energy storage and ultra-fast charge–discharge performance as well as candidate materials for the application of advanced high-temperature pulse capacitors.

Keywords: $K_{0.5}Na_{0.5}NbO_3$ ceramics; microstructure; ultra-fast charge–discharge; energy storage.

1. Introduction

Pure $K_{0.5}Na_{0.5}NbO_3$ (KNN) ceramics, a normal ferroelectric with orthogonal phase structure at room temperature, exhibit a nonlinear polarization response because the polarization of long-range ordered macroscopic ferroelectric domains is easy to saturate at lower electric fields.[1–5] When the applied electric field has been removed, high-residual polarization is presented due to the slow flipping behavior of the macroscopic domain, which leads to large energy loss, low effective energy storage density (W_{rec}) and energy storage efficiency (η) of the KNN ceramic. Therefore, it makes sense to focus on how to effectively optimize the structure and performance of KNN-based ceramic materials to fulfill the development criteria of miniaturization, integration and large capacity of energy storage devices.[2,6–10]

In recent years, researchers have found that KNN-based ceramics can easily achieve sub-micron grain size through component regulation, resulting in increased breakdown field strength and improved energy storage density.[6,9,11–15] For example, Du *et al.*[16,17] obtained sub-micron grain (~0.5 μm) ceramics with high breakdown field strength by introducing the second component and adding sintering aids (CuO, ZnO),[8,13] etc., in which have a high effective energy storage density (2–4 J/cm^3) was achieved, while efficiency was low (<70%), resulting in waste of energy and could not meet commercial requirements. Therefore, in addition to increasing its breakdown field strength E_b, energy storage ceramics must also reduce P_r while keeping high P_{max} in order to obtain materials with a high W_{rec} and η. The generation of residual polarization strength in ferroelectrics has a great relationship with the size of the internal domains, and

[§,**,††]Corresponding authors.

numerous studies have shown that by introducing nonequivalent cations (A = Bi^{3+}, La^{3+}, Sr^{2+}, Sm^{3+}; B = Li^{+}, Ni^{2+}, Mg^{2+}, Sn^{4+}, Zr^{4+})[1,18–24] is conducive to the construction of relaxation ferroelectrics (RFE), induces the generation of polar nanoregions (PNRs), which makes it simpler to return to the initial condition when the applied electric field is removed, this helps to reduce P_r and also enhances the temperature stability and frequency stability of ceramics. Additionally, researches have demonstrated that reducing the size of the ceramic grain can increase its breakdown field strength, thereby increasing the energy storage density.[2,7,9,25,26]

Thus, in this work, $Bi(Mn_{0.5}Ni_{0.5})O_3$ was selected to doped in $K_{0.5}Na_{0.5}NbO_3$ ceramics, and the RFE with submicron grain size of $(1-x)K_{0.5}Na_{0.5}NbO_3-xBi(Mn_{0.5}Ni_{0.5})O_3$ (abbreviated $(1-x)$ KNN-xBMN, x = 0.02, 0.03, 0.04, 0.05, 0.07) were prepared. By raising the breakdown electric field and optimizing polarization intensity, it is expected to obtain KNN-based ferroelectric ceramics with high W_{rec} and η.

2. Experimental Section

2.1. *Sample preparation*

The ceramics of $(1-x)$KNN-xBMN (x = 0, 0.02, 0.03, 0.04, 0.05 and 0.07) were prepared via conventional solid-state method. Raw materials included K_2CO_3 (99.99%), Na_2CO_3 (99.99%), Nb_2O_5 (99.99%), Bi_2O_3 (99.999%), NiO (99.99%) and MnO_2 (99.95%) produced from Sinopharm Chemical Reagent Co., Ltd. In order to reduce the experimental error, the raw materials used in the experiment should be dried in a 120°C air drying oven for 24 h before accurate weighing to remove the moisture in the drugs that are easy to be decomposed by moisture. The dried experimental raw materials were weighed using a balance with 1/10,000 precision, and then poured into the cleaned nylon ball mill tank, then ground for 24 h using ZrO_2 balls and absolute ethanol in a planetary ball mill. The dried slurry was ground into powder and pre-fired in Muffle furnace at 850°C for 5 h to make the ceramics form the main crystalline phase. The powder after pre-firing was subjected to secondary ball milling and the grinding powder was pressed by a powder tablet press into a cylindrical billet with an 11.5 mm diameter and 1.2 mm thickness. Then, the ceramic billet was formed by a cold isostatic press with a pressure of 200–300 MPa and a pressure holding time of 5 min. Finally, the pellets were sinter-fired for 6 h between 1120°C and 1160°C to produce the desired ceramics.

2.2. *Material characterization*

Field emission scanning electron microscopy (FE-SEM, SU-8020, Hitachi, Japan) was used to analyze the microstructures of the KNN-BMN ceramics. The phase structure analysis is based on X-ray diffractometer (XRD, MiniFlex600; Rigaku, Tokyo, Cu-Kα) and laser Raman spectrometer (Almegadispersire, Therm Fisher Nicolet). The samples were prepared for recording the dielectric properties using an LCR meter (Agilent E4980A) and an LCR HiTESTER (HIOKI 3532-50) apparatus by being polished to a thickness of approximately 0.6 mm, coating them with silver electrodes, and firing them at 840°C. A ferroelectric measurement device (TF-2000, Aix ACCT, Aachen, Germany) was used to track the polarization-electric field (P-E) hysteresis loops. The samples had thicknesses of about 0.2 ± 0.05 mm. A commercial dielectric charge-discharge system (Gogo Instrument, CFD-003, Xian, China) was used to test the ceramic capacitor's ability to release energy. A 3 mm diameter Au electrode was affixed, and the samples' thickness was maintained at 0.2 mm for the pulsed measurement.

3. Results and Discussion

3.1. *Phase structure*

The X-ray diffraction pattern of $(1-x)$ KNN-xBMN ceramics at room temperature is depicted in Fig. 1(a). After doping, all samples showed pure perovskite structure, as shown in Fig. 1(a), and the second phase is not generated, indicating that the doped BMN is completely integrated into KNN to generate a new solid solution. Figure 1(b) shows the magnification of the diffraction peak of $(1-x)$ KNN-xBMN ceramics between the peaks of 44° and 48°. It can be found that the diffraction peak near 46° changed significantly after doping, and the double peak of high front and low back of pure KNN ceramics gradually merged into a single peak, as the amount of BMN increases, the peak strength steadily rises and the symmetry improves. It shows that the addition of BMN changes the structure of ceramic phase from normal phase to pseudo cubic phase with good symmetry. In addition, it can be seen that with the increase of doping amount, (200) peak slightly moves to lower angle, this might be caused by the replacement of Nb^{5+} (0.64, CN = 6) in the B location with Ni^{2+} (0.69, CN = 6) having a greater ion radius, resulting in the expansion of the ceramic lattice, thus causing the shift of the diffraction peak.[27]

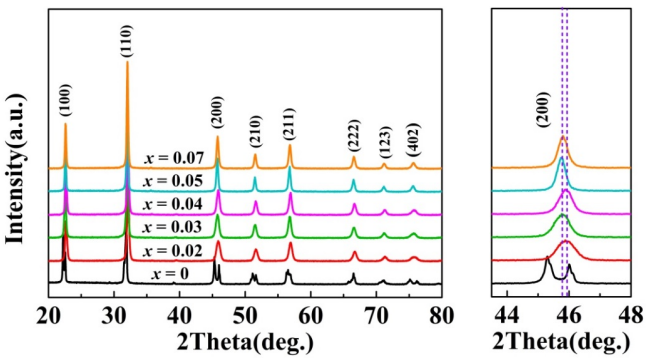

Fig. 1. (a) XRD patterns of $(1-x)$KNN-xBMN ceramics and (b) the enlargement of diffraction peak between 44° and 48°.

The samples were tested using Raman spectroscopy at wavelengths ranging from 100 cm^{-1} to 1000 cm^{-1} in order to better examine the crystal structure of the ceramic samples. As seen in Fig. 2(a), the Raman spectra of $(1-x)$ KNN-xBMN ceramics were at room temperature. The internal deformation of the NbO_6 octahedron inside KNN ceramics is evident in the Raman spectra of each component ceramic, which exhibit six stretching vibration modes ($1A_{1g}(v_1)$, $1E_g(v_2)$, $2F_{1u}(v_3, v_4)$, $F_{2g}(v_5)$ and $F_{2u}(v_6)$).[28,29] The peak strength of the Raman peak corresponding to the $E_g(v_2)$ stretching vibration mode rapidly decreased as BMN content increased. As the Nb–O bond stretches, the vibration modes of $E_g(v_2)$ and $A_{1g}(v_1)$ between 550 cm^{-1} and 610 cm^{-1} reflect these changes and the shift of their Raman peaks can reflect the changes of the internal structure of ceramic.[28–30] Gaussian fitting is used to fit in the range of 450–750 cm^{-1} of ceramic. Figures 2 (b)–2(f), respectively, show the results of Gaussian fitting of Raman peaks in the range of 450–750 cm^{-1} for $(1-x)$ KNN-xBMN ceramics. With the increase in BMN content, the Raman peak of $A_{1g}(v_1)$ gradually shifted to the lower band, decreasing from 611.6 cm^{-1} at $x = 0.02$–607.8 cm^{-1}. At $x = 0.07$, it demonstrated the improved symmetry and a reduction in distortion in the NbO_6 octahedron. It is further confirmed that the introduction of BMN changes the structure of ceramic phase from orthotropic phase to more symmetric pseudo-cubic phase.

3.2. *Microstructure*

The natural surface of $(1-x)$ KNN-xBMN ceramics is depicted in the SEM image in Figs. 3(a)–3(e) at the optimal sintering temperature. It shows that the grains of all components are full, showing regular square blocks tightly packed together and the grain boundaries are relatively clear, indicating that the prepared ceramics have good compactness and compared with pure KNN ceramics, the ceramic grains are significantly reduced after doping. To further understand how BMN doping affects the grain size of KNN-based ceramics, the grain size distribution of doped ceramics was computed using the Nano Measurer software. Figures 4(a)–4(f) depict a bar chart of the grain size distribution of $(1-x)$ KNN-xBMN ceramics. Figure 4(f) demonstrates that when the component content increases following doping, the average grain size of each component initially reduces and then increases. The ceramic grain is at its smallest size of 118 nm at $x = 0.05$. All of the ceramic grains were smaller than 150 nm after doping, suggesting that the use of BMN might inhibit the growth of ceramic grains.

3.3. *Dielectric properties*

The permittivity and dielectric loss curves of $(1-x)$ KNN-xBMN ceramics at various frequencies as a function of temperature are shown in Figs. 5(a)–5(e). It is shown that the dielectric temperature spectrum of all components exhibits a dielectric peak as test temperature rises, indicating that only

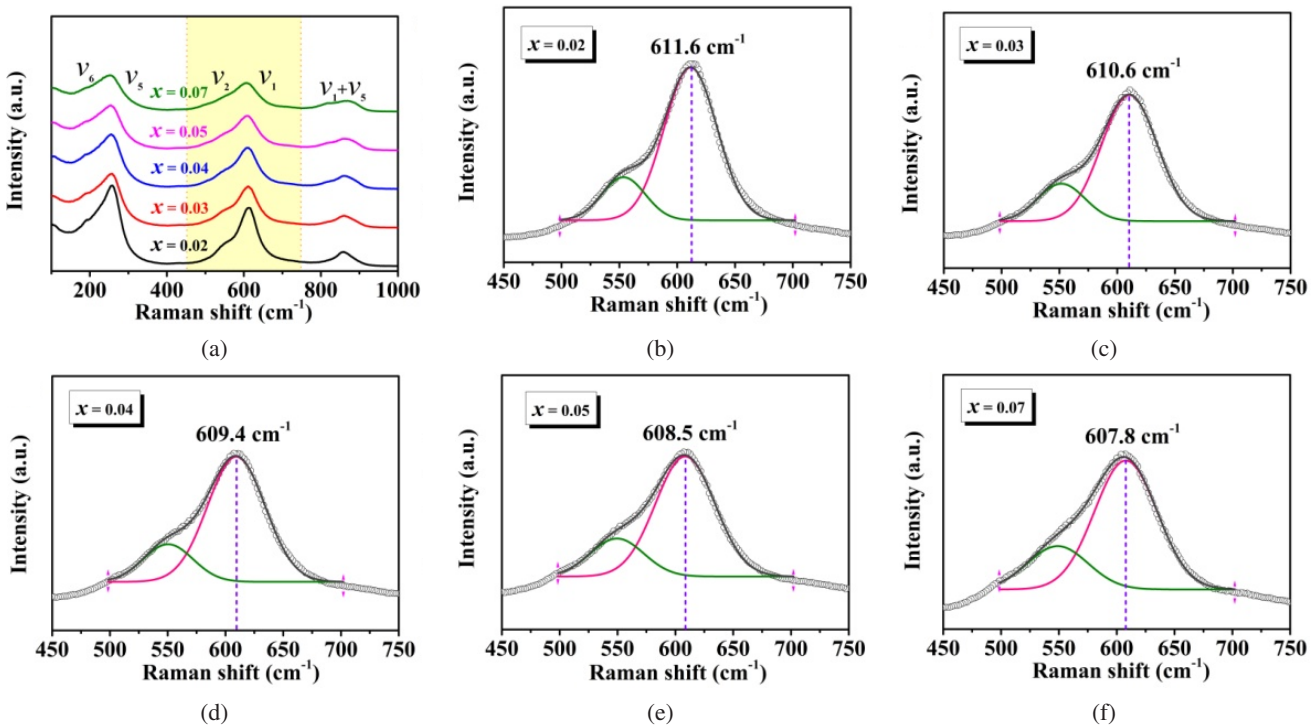

Fig. 2. (a) Raman spectra of $(1-x)$KNN-xBMN ceramics measured at room temperature; enlarged Raman spectra in the wavelength range of 450–750 cm^{-1} and Gaussian fitting peak results: (b) $x = 0.02$, (c) $x = 0.03$, (d) $x = 0.04$, (e) $x = 0.05$ and (f) $x = 0.07$.

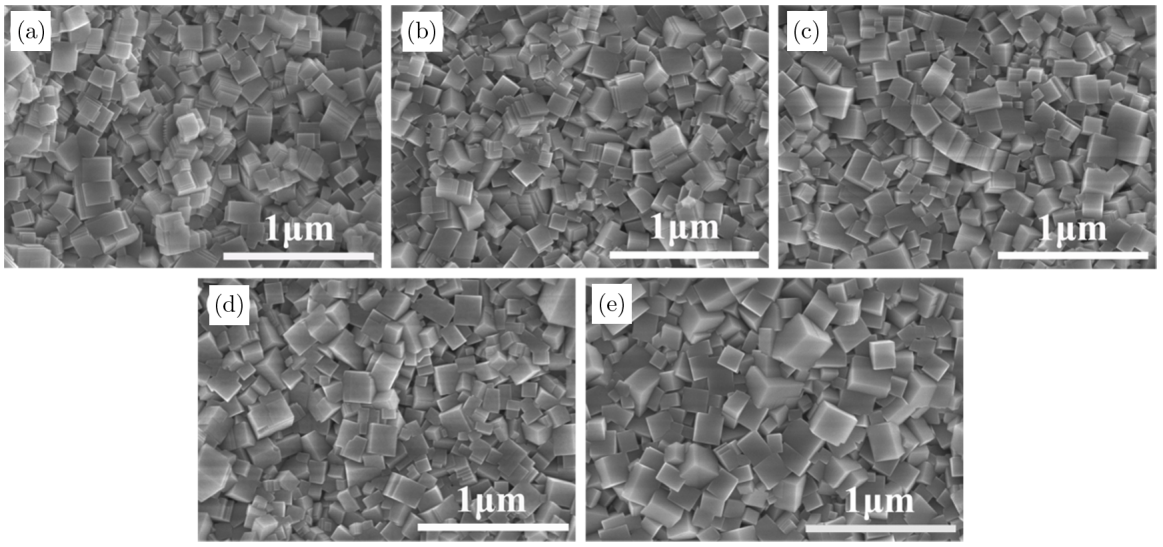

Fig. 3. Scanning electron microscope images of the natural surface of $(1-x)$KNN-xBMN ceramics: (a) $x = 0.02$, (b) $x = 0.03$, (c) $x = 0.04$, (d) $x = 0.05$ and (e) $x = 0.07$.

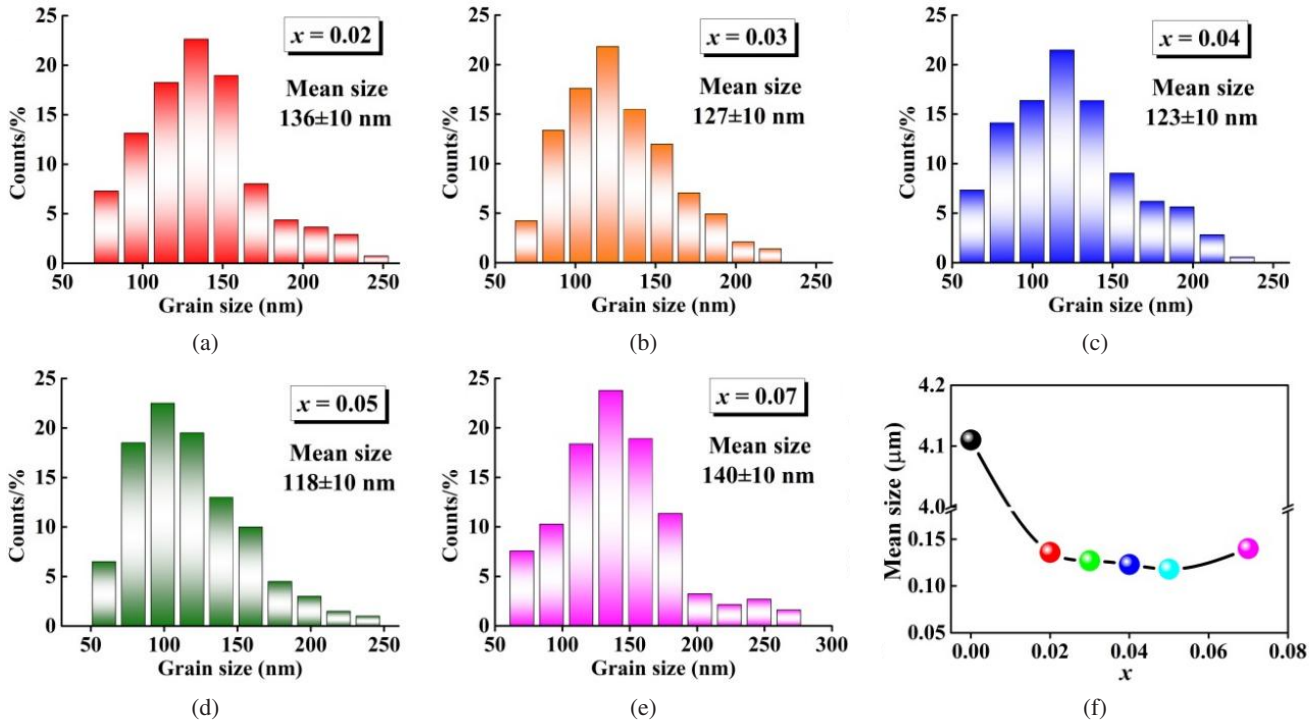

Fig. 4. (a) The histogram of grain size distribution for $(1-x)$KNN-xBMN ceramics: (a) $x = 0.02$, (b) $x = 0.03$, (c) $x = 0.04$, (d) $x = 0.05$, (e) $x = 0.07$ and (f) graph of average grain size changing with component content.

one phase transition occurs with the increase of temperature, that is, after BMN doping at room temperature, the ceramics become cubic in structure as seen by the transition from the pseudo-cubic phase to the cubic phase. The dielectric properties of the doped ceramics deteriorate when compared to pure KNN, and the dielectric constants are all less than 1600. This phenomenon is caused by a reduction in the size of the ceramic grain. The grain boundary has a small dielectric constant, and as grain size decreases, the grain boundary will increase, causing the ceramic dielectric properties to deteriorate. Furthermore, Figs. 5(a)–5(e) show that the ceramics have good dielectric frequency stability. The dielectric curves of the ceramics at the test frequencies of 50 kHz, 100 kHz and 200 kHz almost completely coincide, and the dielectric loss of the samples is less than 0.05 in the range of 30–350°C, which is conductive to the improvement of the η value of the

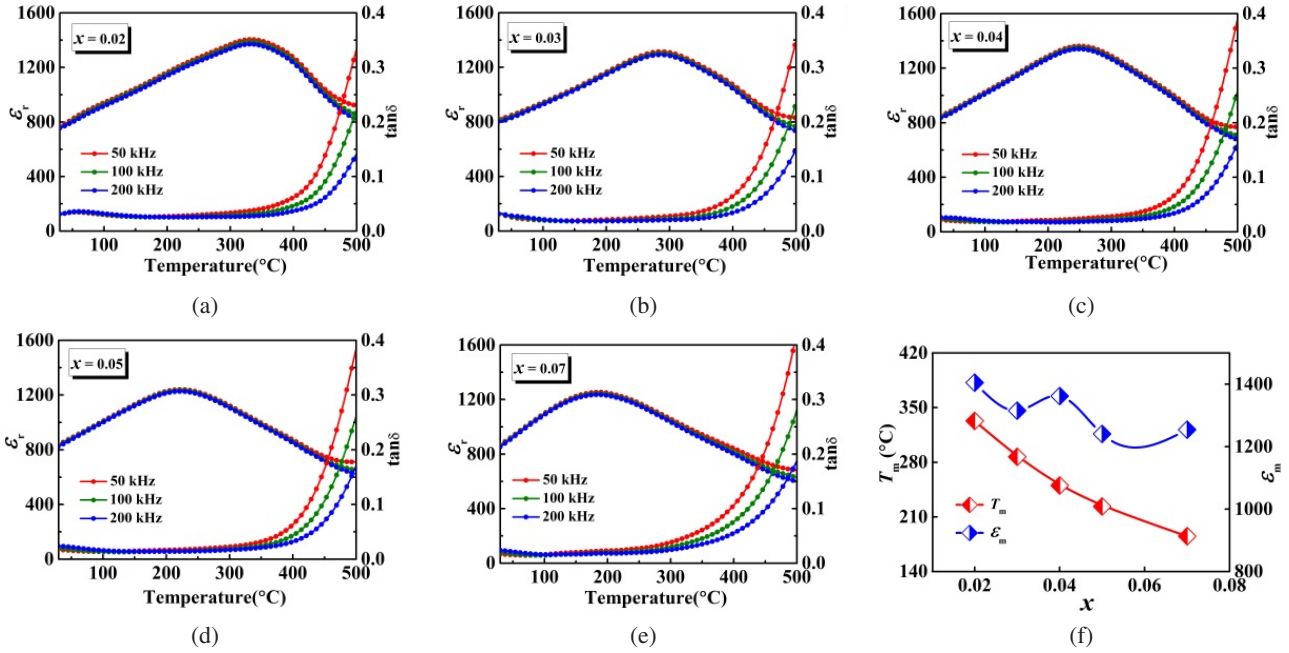

Fig. 5. Dielectric temperature spectrum of $(1-x)$KNN-xBMN ceramics at different frequencies: (a) $x = 0.02$, (b) $x = 0.03$, (c) $x = 0.04$, (d) $x = 0.05$, (e) $x = 0.07$ and (f) the value of ε_m and T_m at the frequency of 50 kHz for $(1-x)$KNN-xBMN ceramics.

ceramics. Figure 5(f) displays the maximum permittivity and Curie temperature of ceramics made of $(1-x)$ KNN-xBMN at 50 kHz. It is shown that with the increase in BMN content, Curie temperature steadily advances in the direction of low temperatures, whereas the maximum permittivity only slightly shifts from 1405 at $x = 0.02$–1254 at $x = 0.07$. This suggests that the dielectric constant of BMN is not greatly affected by its composition.

According to the dielectric temperature spectrum in Fig. 5, it is shown that the introduction of BMN promoted the Curie temperature of ceramics to gradually move to low temperature, and the dielectric peak gradually broadened and changed gently, showing the relax-like behavior of the diffusion phase transition. To continue investigating the relaxation behavior, the Curie–Weiss law is employed to define the deviation level of the Curie temperature[31–33]:

$$\frac{1}{\varepsilon_r} = \frac{T - T_0}{C}, \tag{1}$$

where C represents the Curie–Weiss constant, and T_0 represents the Curie–Weiss temperature. For ferroelectrics, when the temperature T is higher than Burns temperature T_B, the permittivity and temperature conform to this law, but for relaxation ferroelectrics, when T is lower than T_B (initiation nucleation temperature during PNRs cooling), it will shift, which proves the existence of dispersion phase transition in ceramics. Usually, the difference between T_B and T_m, ΔT, is used to represent the degree of deviation, and the larger ΔT indicates the more obvious dispersion phase transition behavior.[34,35] Figures 6(a)–6(e) show the curve of $10^3/\varepsilon_r$ with temperature at 50 kHz frequency, and the fitting result and the curve of T_B, T_m and ΔT of each component ceramic with x are shown in Fig. 6(f). As shown in Fig. 6(f), as the amount of BMN grew, both T_B and T_m gradually decreased, T_m decreased more obviously, and ΔT gradually increased, demonstrating that the dispersion relaxation degree of ceramics was enhanced.

The test range is 40–10^7 Hz, the variation of dielectric properties of ceramics with different BMN doping amounts as a function of frequency in Fig. 7(a). As can be seen from Fig. 7(a), when the test frequency rises from 40 Hz to 10^7 Hz, the permittivity of all components tends to decrease, and the change rate of permittivity of each component is shown in Fig. 7(b). It can be found that compared with the permittivity of 10 kHz, the change rate is between −10–30%. When the test frequency is greater than 1 kHz, the change rate is less than 10%. All samples have a dielectric loss of less than 0.1, which is significant at low frequencies but tends to stabilize and fall below 0.05 at 1 kHz. The outcomes demonstrate that the ceramics with BMN doping have good dielectric frequency stability.

3.4. *Energy storage properties*

Figures 8(a)–8(e) show the monopolar P-E curves of samples under different electric fields, the test frequency is 10 Hz, and P_{max}, P_r and E_b under the critical breakdown field strength of each component ceramic are shown in Fig. 8(f). The hysteresis loop of doped ceramics gradually becomes thinner as the doping amount increases are shown in Figs. 8 (a)–8(e). When $x = 0.07$, P_r decreases to 2.37 μC/cm^2, indicating that

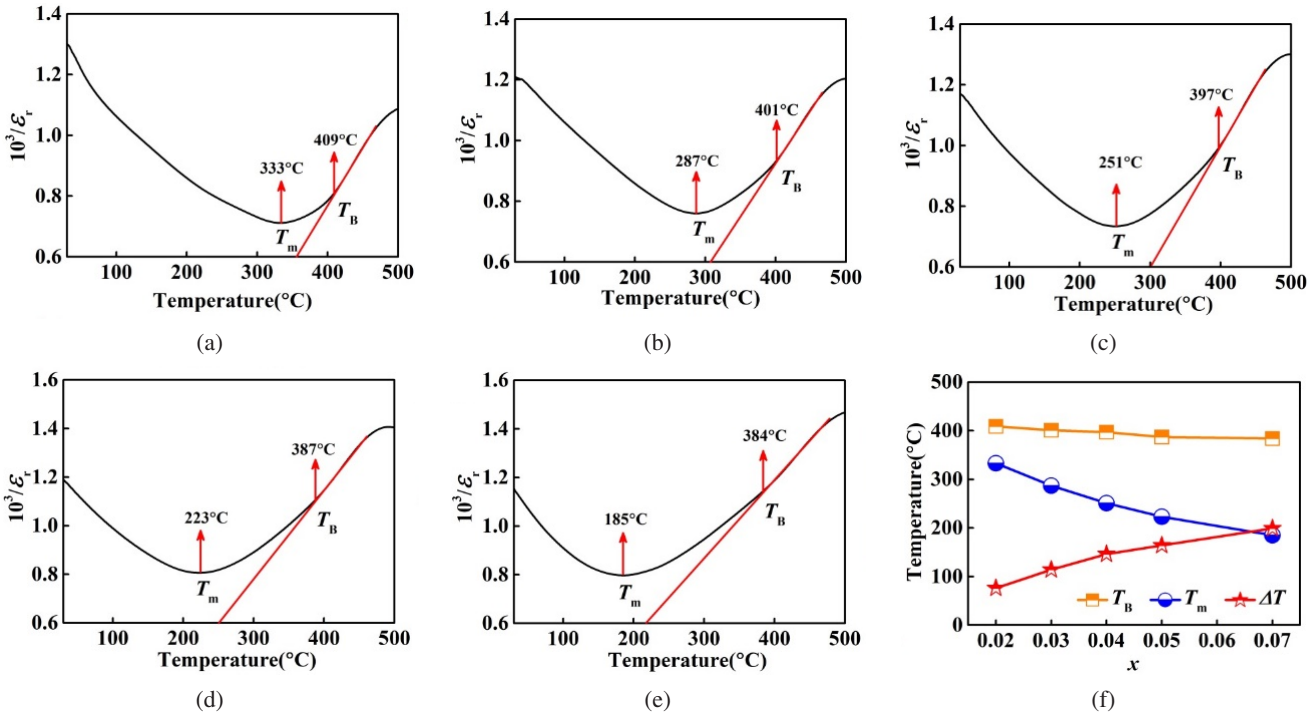

Fig. 6. The relation of $10^3/\varepsilon_r$ and temperature: (a) $x = 0.02$, (b) $x = 0.03$, (c) $x = 0.04$, (d) $x = 0.05$, (e) $x = 0.07$; (f) the value of T_B, T_m and ΔT at the frequence of 50 kHz for $(1 - x)$KNN-xBMN ceramics.

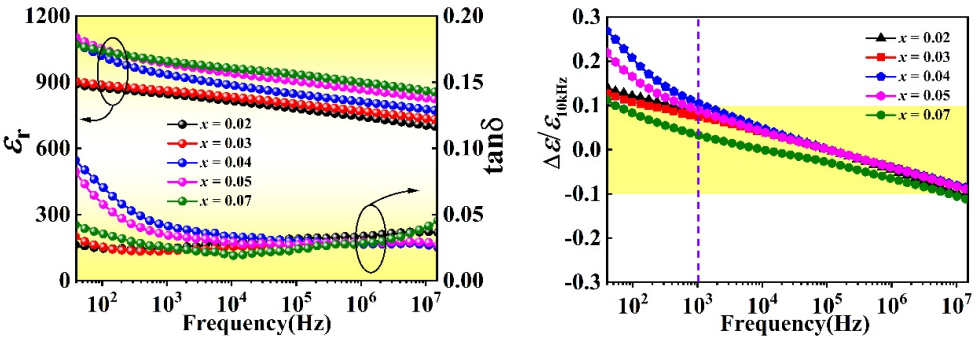

Fig. 7. (a) Dielectric properties of $(1 - x)$KNN-xBMN ceramics at room temperature as a function of frequency and (b) frequency stability of dielectric constant of ceramics.

the introduction of BMN makes ceramics gradually transform into relaxation ferroelectrics, which is conducive to improving their W and η values. Compared with pure KNN, the breakdown field strength of ceramic has also been greatly improved. After doping, the breakdown field strength of all the component of ceramics is greater than 160 kV/cm. As the quantity of doping grows, the breakdown field strength first rises and then falls. This fact explains the majority of the increase in the breakdown electric field with decreasing ceramic grain size following doping, which reaches a maximum value of 240 kV/cm at $x = 0.04$.

To further explore the energy storage properties of 0.96 KNN-0.04 BMN ceramics, the monopolar P-E curves of 0.96 KNN-0.04 BMN ceramics measured at room temperature at 10 Hz and different electric fields are shown in Fig. 9(a). 0.96 KMN-0.04 BMN ceramics all show fine monopolar P-E hysteresis loop under all test electric fields. P_{max} of the sample grows quickly as the applied test electric field is increased. The high P_{max} (25.2 μC/cm^2) is obtained at the critical breakdown field strength of 240 kV/cm, while P_r increases slightly. When the electric field strength increases from 40 kV/cm to 240 kV/cm, the P_r value increases from 0.42 μC/cm^2 to 2.53 μC/cm^2. Figure 9(b) summarizes the W_{total}, W_{rec} and η of 0.96 KNN-0.04 BMN ceramics under various electric fields. With the applied electric field being increased, W_{total} and W_{rec} are greatly improved. The W_{total} value climbed from 0.148 J/cm^3 to 2.358 J/cm^3 and the W_{rec} value increased from 0.115 J/cm^3 to 1.826 J/cm^3 when the electric field strength increased

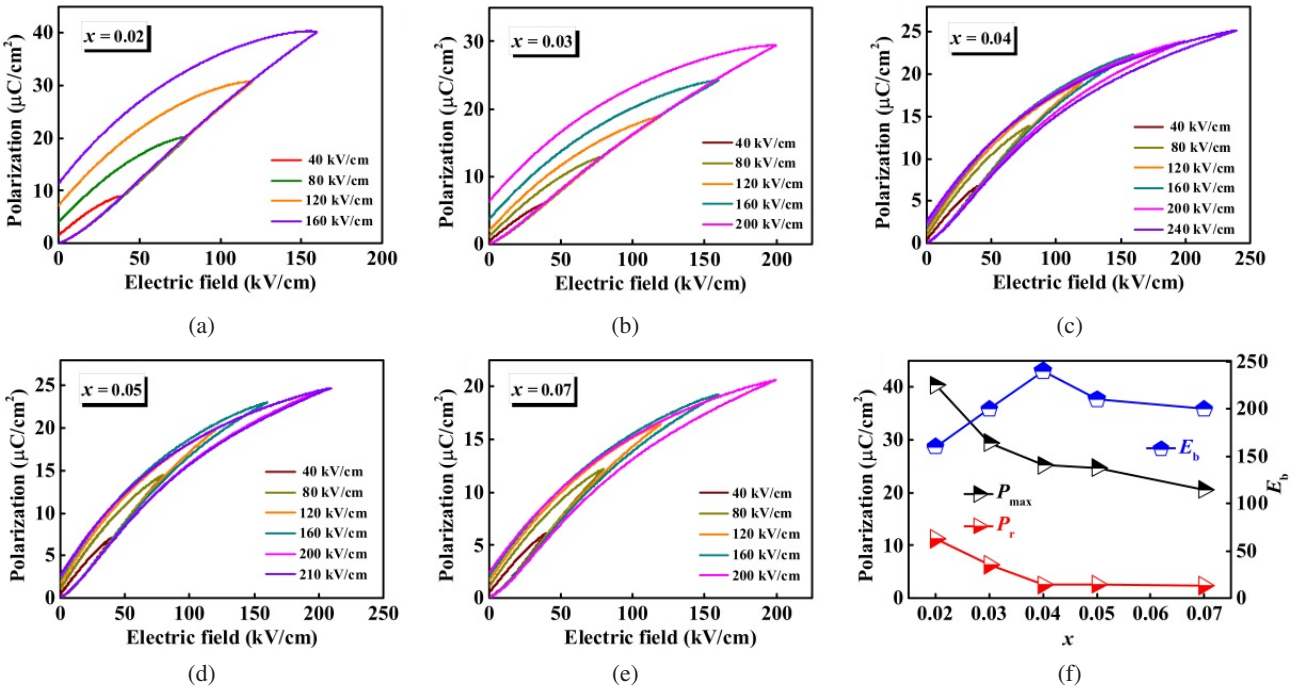

Fig. 8. Unipolar *P-E* loops of $(1-x)$KNN-xBMN ceramics at the frequence of 10 Hz with different electric fields: (a) $x = 0.02$, (b) $x = 0.03$, (c) $x = 0.04$, (d) $x = 0.05$, (e) $x = 0.07$; (f) the value of P_{max}, P_r and E_b of $(1-x)$KNN-xBMN ceramics under their critical breakdown field strength.

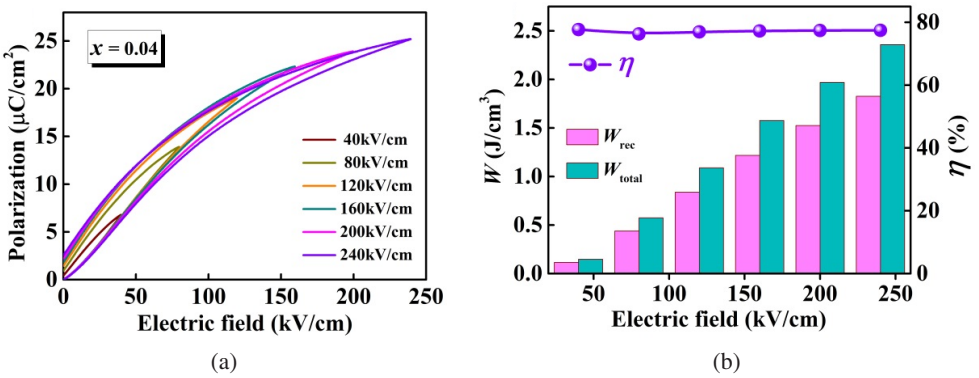

Fig. 9. (a) Unipolar P-E loops and (b) W_{total}, W_{rec} and η of 0.96KNN-0.04BMN ceramics with different electric fields.

from 40 kV/cm to 240 kV/cm. It is worth noting that the η of 0.96 KNN-0.04 BMN ceramics almost does not change with the electric field, which keeps in the range of 76.3–77.7%, and the change rate is less than 1.8%, demonstrating that the ceramics have excellent electric field stability.

Another crucial element in the use of energy storage media materials is good stability throughout a broad frequency range of operation. Figure 10(a) illustrates the monopolar *P-E* curve of 0.96 KNN-0.04 BMN ceramics in the frequency range of 1–500 Hz with an applied electric field of 150 kV/cm. It can be found that as test frequency is increased, the shape of the monopolar *P-E* curve basically remains unchanged. Due to the slow response of the electrical domain inside the ceramic at high frequency, the saturation polarization intensity P_{max} decreases slightly at high frequency, from 22.20 μC/cm^2 at 1 Hz to 19.20 μC/cm^2 at 500 Hz. The findings demonstrate that the energy storage characteristics of 0.96KNN-0.04BMN ceramics fluctuate slightly with the change of test frequency, and W_{total} and W_{rec} decrease from 1.51 J/cm^3 and 1.07 J/cm^3 to 1.35 J/cm^3 and 0.94 J/cm^3 with the increase of frequency, respectively. The change rate is 10.6% and 11.8%, which is mainly caused by the decrease of the P_{max} value, this is primarily due to the decline in P_{max} value, but the change rate of η is just 6.1%, demonstrating good overall frequency stability.

In addition, the ceramic capacitors in practical application need to have good fatigue resistance to ensure that the devices have a long service life and can be used in a long-term charge and discharge cycle. The energy storage and anti-fatigue dependence performance of the monopolar *P-E* curves of 0.96 KNN-0.04 BMN ceramics are shown in Figs. 10(c) and

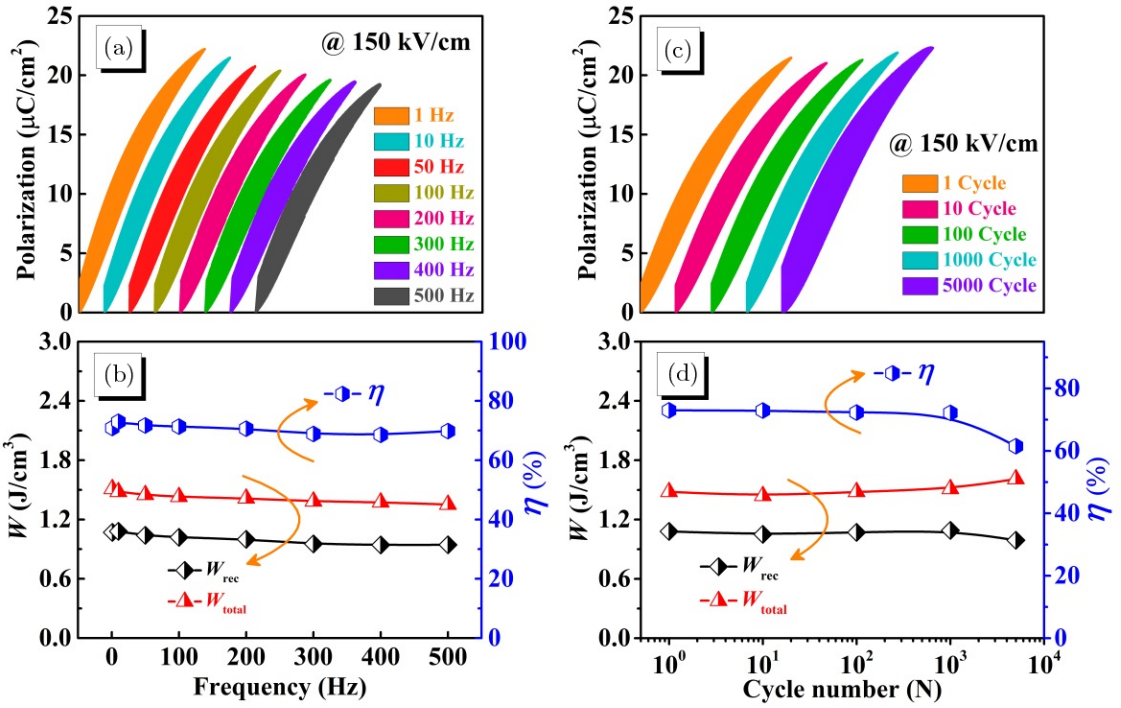

Fig. 10. (a) Unipolar *P-E* loops of 0.96KNN-0.04BMN ceramics at various frequencies measured under 150 kV/cm, (b) W_{total}, W_{rec} and η calculated through (a); (c) unipolar *P-E* loops of 0.96KNN-0.04BMN ceramics at different cycles measured under 150 kV/cm, (d) W_{total}, W_{rec} and η calculated through (c).

10(d), respectively. The test electric field is 150 kV/cm, and the number of cycles is 1–5000. As shown in Fig. 10(c), when the number of cycles is less than or equal to 1000, the *P-E* curve of ceramic almost does not change with the increase of the number of cycles, while P_{max} and P_r have no obvious trend of change, indicating that their polarization response characteristics are insensitive. The calculated change rates of W_{total}, W_{rec} and η are 4.6%, 3.7% and 1.1%, respectively. When the number of cycles reaches 5000, the increase of the P_{max} value makes the W_{total} of the ceramic increase slightly, but due to the large increase of P_r, the decrease of W_{rec} and η is more obviously, the rate of change is 8.3% and 15.8%, respectively, in general, the 0.96KNN-0.04BMN ceramic shows superior anti-fatigue characteristics.

Current pulse power systems require ceramic capacitors not only to have excellent energy storage performance, but also to have high power density. Therefore, under damped conditions, the influence of the electric field on the discharge performance of 0.96 KNN-0.04 BMN ceramics is investigated, as shown in Fig. 11(a). As can be seen from the figure, the sample displayed a similar current-time curve as the test electric field increased, and the discharge period was stable at about 61 ns. When the electric field was increased, the peak value of first current increased as well, and the value increased from 5.23 A at 20 kV/cm to 38.82 A at 160 kV/cm.

In addition, the position of the current peak moves as the electric field increases, indicating the voltage and current are also not linear.[36,37] The electric field and the relationship between the ceramic's current density C_D and power density P_D are shown in Fig. 11(b), where C_D and P_D values have grown greatly from 166.56 A/cm² and 1.67 MW/cm³ to 1236.31 A/cm² and 98.90 MW/cm³, respectively. Figures 11(c) and 11(d) show the under-damped discharge current curve of the 0.96KNN-0.04BMN ceramic measured at an electric field of 160 kV/cm from 30°C to 180°C and the corresponding C_D and P_D values, respectively. Due to the leakage loss of the capacitor at high temperature, the sum value of the ceramic will be slightly reduced at high temperature, but the rate of change is less than 3%, and the ceramic shows excellent temperature stability, which further expands the application field of the ceramic.

Efficient and stable charge–discharge performance is also a key performance parameter to evaluate the commercial value of pulse power capacitors, in order to explore the pulse discharge energy density and discharge time of ceramics in practical applications, the discharge of ceramics 0.96KNN-0.04BMN in the overdamped state was tested by using a load resistance of 300 Ω (the actual resistance is 302 Ω). Figure 12(a) depicts the room-temperature overdamped discharge curve of 0.96KNN-0.04BMN ceramic under various electric fields. It is evident that the discharge current peaks fast and grows progressively with increasing electric field strength, reaching a maximum of 8.6 A when the electric field is supplied at 160 kV/cm. Figure 12(b) plots the integrated discharge energy density W_D versus time for an electric field of 20–160 kV/cm, and the dashed line $t_{0.9}$ represents

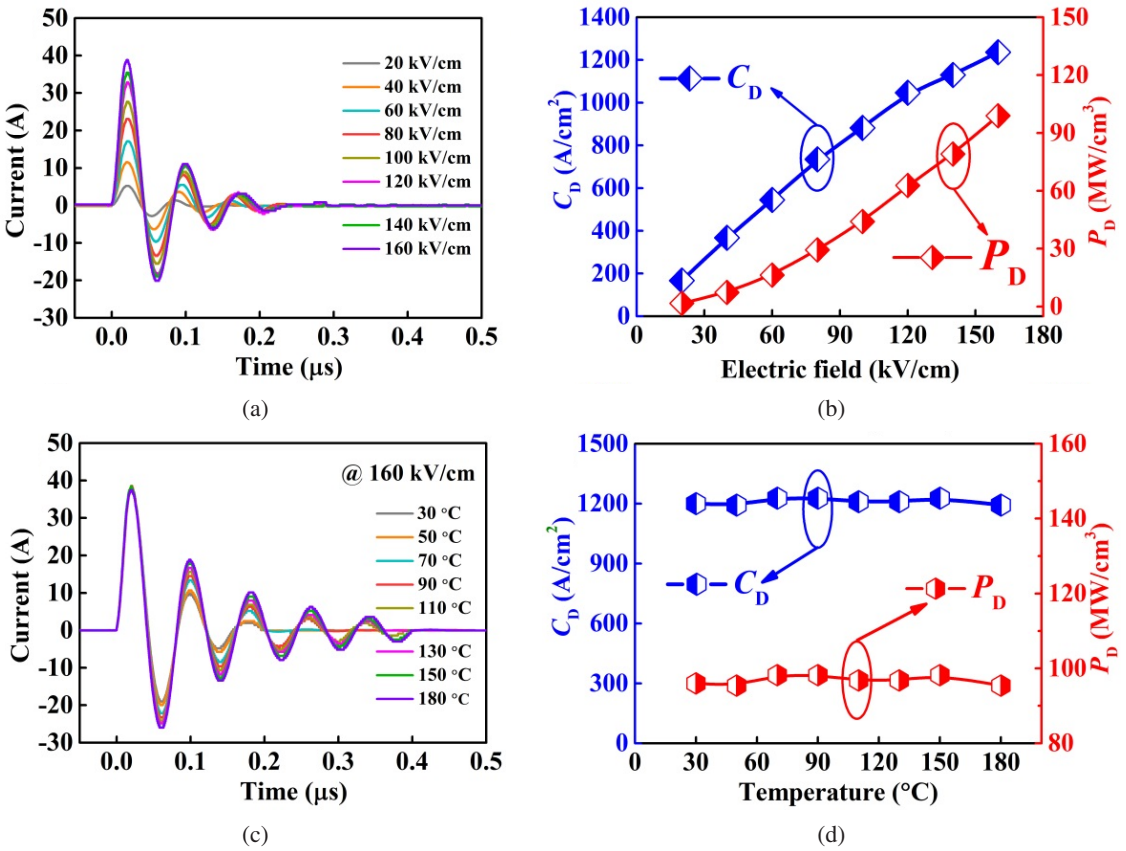

Fig. 11. (a) Underdamped charge–discharge curves under various electric fields, (b) C_D and P_D versus electric field of 0.96KNN-0.04BMN ceramics; (c) Underdamped charge–discharge curves at different temperatures, (d) C_D and P_D at various different of 0.96KNN-0.04BMN ceramics measured under 160 kV/cm.

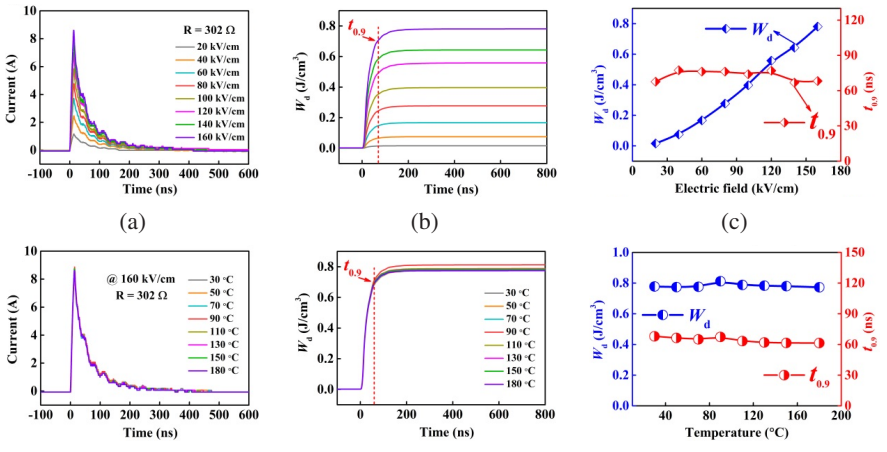

Fig. 12. (a) Overdamped discharge curves under various electric fields, (b) W_D as a function of time at various electric field, (c) W_D and $t_{0.9}$ at various electric field of the 0.96KNN-0.04BMN ceramics; (d) overdamped discharge curves at different temperatures, (e) time dependence of W_D at various temperatures, (f) W_D and $t_{0.9}$ at different temperatures of 0.96KNN-0.04BMN ceramics under 160 kV/cm.

the amount of time needed to reach 90% of the maximum W_D value (usually expressing the speed of discharge). The curves for W_D and $t_{0.9}$ as the electric field changed are summarized in Fig. 12(c), and the W_D value increased with increasing electric field strength, reaching 0.781 J/cm^3 at 160 kV/cm. However, the fluctuation as a function of the electric field is minimal — less than 80 ns — and the discharge rate will be faster under the influence of high electric field, requiring only 68.2 ns (160 kV/cm). In addition, the thermal stability of the discharge performance of 0.96KNN-0.04BMN ceramics in the

overdamped state was also tested, and the overdamped discharge curve shown in Fig. 12(d) almost did not change with the rise of temperature, and the discharge current reached its maximum value at 14 ns, stabilized at 8.7±0.1 A, and the rate of change in the range of 30–180°C was less than 2%, indicating that it had good thermal stability. Figures 12(e) and 12(f) also show the change law of discharge energy density W_D and discharge time $t_{0.9}$ at different temperatures, and it can be found that the change of W_D and $t_{0.9}$ in the figure is very small, and the available rates of change are 4.8% and 9.7%, respectively, showing superior temperature stability in a wide temperature range (30–180°C).

4. Conclusions

We designed to introduce BMN into KNN to improve the polarization strength of ceramics, so as to improve the energy storage characteristics of ceramics, and we systematically studied the effects of phase structure, microscopic grain size and dielectric relaxation on its energy storage performance, and evaluated the frequency stability, fatigue resistance and charge–discharge behavior of its energy storage performance. BMN doping level of 0.04, 0.96KNN-0.04BMN ceramic obtained good energy storage performance with acceptable energy storage density W_{rec} of 1.826 J/cm^3 and efficiency η of 77.4%, as well as good frequency stability (1–500 Hz) and fatigue resistance (1–5000 cycles), making the ceramic a desirable substance for applications requiring temperature-stable dielectric capacitors.

Acknowledgment

This work was supported by the National Natural Science Foundation of China (NSFC) (Grant No. 52272119, 51872177). The authors would also like to thank the Natural Science Basic Research Plan in the Shaanxi Province of China (Grant No. 2021ZDLSF06-03, 2021JM-201), the Fundamental Research Funds for the Central Universities (Program No. GK202002014) and the Fondamental Innovation Project in School of Materials Science and Engineering (SNNU).

References

[1]W. B. Li *et al*., Novel barium titanate based capacitors with high energy density and fast discharge performance, *J. Mater. Chem. A* **5**, 19607 (2017).
[2]B. Chen *et al*., Ultrahigh storage density achieved with $(1-x)$ KNN-xBZN ceramics, *J. Eur. Ceram. Soc.* **40**, 2936 (2020).
[3]X. Wang *et al*., Giant piezoelectricity in potassium-sodium niobate lead-free ceramics, *J. Am. Chem. Soc.* **136**, 2905 (2014).
[4]T. Zheng *et al*., Recent development in lead-free perovskite piezoelectric bulk materials, *Prog. Mater. Sci.* **98**, 552 (2018).
[5]X. Zhang *et al*., Giant energy density and improved discharge efficiency of solution-processed polymer nanocomposites for dielectric energy storage, *Adv. Mater.* **28**, 2055 (2016).
[6]Z., Yang *et al*., Significantly enhanced recoverable energy storage density in potassium–sodium niobate-based lead free ceramics, *J. Mater. Chem. A* **4**, 13778 (2016).
[7]Q. Chai *et al*., Lead-free (K,Na)NbO_3-based ceramics with high optical transparency and large energy storage ability, *J. Am. Ceram. Soc.* **101**, 2321 (2018).
[8]B. Qu *et al*., Large recoverable energy storage density and low sintering temperature in potassium-sodium niobate-based ceramics for multilayer pulsed power capacitors, *J. Am. Ceram. Soc.* **100**, 1517 (2017).
[9]Z. Yang *et al*., Grain size engineered lead-free ceramics with both large energy storage density and ultrahigh mechanical properties, *Nano Energy* **58**, 768 (2019).
[10]M. Zhang *et al*., Excellent energy density and power density achieved in $K_{0.5}Na_{0.5}NbO_3$-based ceramics with high optical transparency, *J. Alloys Compd.* **829**, 154565 (2020).
[11]H. Cheng *et al*., Enhanced dielectric relaxor properties in $(1-x)(K_{0.5}Na_{0.5})NbO_3 - x(Ba_{0.6}Sr_{0.4})_{0.7}Bi_{0.2}TiO_3$ lead-free ceramic, *J. Alloys Compd.* **579**, 192 (2013).
[12]R. Kumar and S. Singh, Enhanced electrocaloric response and high energy-storage properties in lead-free $(1-x)$ $(K_{0.5}Na_{0.5})NbO_3$ - $x$$SrZrO_3$ nanocrystalline ceramics, *J. Alloys Compd.* **764**, 289 (2018).
[13]B. Qu *et al*., Enhanced dielectric breakdown strength and energy storage density in lead-free relaxor ferroelectric ceramics prepared using transition liquid phase sintering, *RSC Adv.* **6**, 34381 (2016).
[14]H. Tao *et al*., Optimization of energy storage density in relaxor (K, Na, Bi)NbO_3 ceramics, *J. Mater. Sci.* **28**, 16199 (2017).
[15]H. Sun *et al*., (K,Na)NbO_3 ferroelectrics: A new class of solid-state photochromic materials with reversible luminescence switching behavior, *J. Mater. Chem. C* **5**, 9080 (2017).
[16]T. Shao *et al*., Potassium–sodium niobate based lead-free ceramics: Novel electrical energy storage materials, *J. Mater. Chem. A* **5**, 554 (2017).
[17]B. Qu *et al*., Lead-free relaxor ferroelectric ceramics with high optical transparency and energy storage ability, *J. Mater. Chem. C* **4**, 1795 (2016).
[18]F. Si *et al*., Enhanced energy storage and fast charge-discharge properties of $(1-x)BaTiO_3 - xBi(Ni_{1/2}Sn_{1/2})O_3$ relaxor ferroelectric ceramics, *Ceram. Int.* **45**, 17580 (2019).
[19]F. Si *et al*., A new type of $BaTiO_3$-based ceramics with $Bi(Mg_{1/2}Sn_{1/2})O_3$ modification showing improved energy storage properties and pulsed discharging performances, *J. Alloys Compd.* **819**, 153004 (2020).
[20]T. Wang *et al*., Relaxor ferroelectric $BaTiO_3$-$Bi(Mg_{2/3}Nb_{1/3})O_3$ ceramics for energy storage application, *J. Am. Ceram. Soc.* **98**, 559 (2015).
[21]M. Zhou *et al*., Combining high energy efficiency and fast charge-discharge capability in novel $BaTiO_3$-based relaxor ferroelectric ceramic for energy-storage, *Ceram. Int.* **45**, 3582 (2019).
[22]X. Nie *et al*., High transparency and good electric properties in low symmetry BNT-based ceramics, *Solid State Sci.* **129**, 106906 (2022).
[23]Z. Peng *et al*., A new family of high temperature stability and ultra-fast charge–discharge KNN-based lead-free ceramics, *J. Mater. Sci.* **57**, 9992 (2022).
[24]J. Wang *et al*., Ultra-fast charge-discharge and high energy storage density realized in $NaNbO_3$–$La(Mn_{0.5}Ni_{0.5})O_3$ ceramics, *Ceram. Int*. **47**, 28493 (2021).
[25]G. Liu *et al*., Energy storage properties of bismuth ferrite based ternary relaxor ferroelectric ceramics through a viscous polymer process, *Chem. Eng. J.* **412**, 127555 (2021).

[26]W. Lv *et al*., Significantly improved energy storage performance of NBT-BT based ceramics through domain control and preparation optimization, *Chem. Eng. J.* **420**, 129900 (2021).
[27]R. Shi *et al*., A novel lead-free $NaNbO_3$–$Bi(Zn_{0.5}Ti_{0.5})O_3$ ceramics system for energy storage application with excellent stability, *J. Alloys Compd.* **815**, 152356 (2020).
[28]M. Peddigari *et al*., Dielectric and variable range hopping nature of Gd_2O_3-doped $K_{0.5}N_{0.5}NbO_3$ piezoelectric ceramics, *AIP Adv*. **5**, 107129 (2015).
[29]W. L. Zhu *et al*., Structural characteristics of Mg-doped $(1 - x)(K_{0.5}Na_{0.5})NbO_3 - xLiSbO_3$ lead-free ceramics as revealed by Raman spectroscopy, *J. Phys. D. Appl. Phys.* **44**, 505303 (2011).
[30]F. Rubio-Marcos *et al*., Correlation between the piezoelectric properties and the structure of lead-free KNN-modified ceramics studied by Raman spectroscopy, *J. Raman Spectrosc.* **42**, 639 (2011).
[31]J. Li *et al*., Effects of long- and short-range ferroelectric order on the electrocaloric effect in relaxor ferroelectric ceramics, *Phys. Rev. Lett.* **11**, 044032 (2019).
[32]W. Cai *et al*., Effect of hafnium on the microstructure, dielectric and ferroelectric properties of $Ba(Zr_{0.2}Ti_{0.8})O_3$ ceramics, *Ceram. Int*. **38**, 3367 (2012).
[33]P. Zhao *et al*., Novel Ca doped $Sr_{0.7}Bi_{0.2}TiO_3$ lead-free relaxor ferroelectrics with high energy density and efficiency, *JEur. Ceram. Soc.* **40**, 1938 (2020).
[34]X. G. Tang *et al*., Diffuse phase transition and dielectric tunability of $Ba(Zr_yTi_{1-y})O_3$ relaxor ferroelectric ceramics, *Acta Mater.* **52**, 5177 (2004).
[35]F. Li *et al*., Local structural heterogeneity and electromechanical responses of ferroelectrics: Learning from relaxor ferroelectrics, *Adv. Funct. Mater*. **28**, 1801504 (2018).
[36]L. Zhang *et al*., Novel $Na_{0.5}Bi_{0.5}TiO_3$ based, lead-free energy storage ceramics with high power and energy density and excellent high-temperature stability, *Chem. Eng. J.* **383**, 123154 (2020).
[37]M. Zhou *et al*., Novel sodium niobate-based lead-free ceramics as new environment-friendly energy storage materials with high energy density, high power density, and excellent stability, *ACS Sustain. Chem. Eng.* **6**, 12755 (2018).